

# The Color Dipole Picture and extracting the ratio of structure functions at small $x$

B.Rezaei\* and G.R.Boroun†

*Physics Department, Razi University, Kermanshah 67149, Iran*

(Dated: December 21, 2024)

We present a set of formulas to extract the ratio  $F_L(x, Q^2)/F_2(x, Q^2)$  and  $R(x, Q^2)$  from the  $F_2(x, Q^2)$  parameterization in the next-to-next-to-leading order of the perturbative theory at low  $x$  values. The behavior of these ratios studied in comparison with the fixed and effective exponents with respect to the power-law behavior of the proton structure function. The results are compared with the experimental data and the color dipole model bounds. These ratios are in good agreement with the DIS experimental data throughout the fixed value of the invariant mass. The behavior of these ratios controlled by the nonlinear corrections at low values of  $Q^2$ . These results within the next-to-next-to-leading order approximation can be applied in the LHeC region for analyses of ultra-high energy processes in a wide range of  $Q^2$  values.

## Introduction

Deep inelastic scattering (DIS) at low values of the Bjorken variable  $x$  can be described in terms of the imaginary part of forward Compton-scattering amplitude. For  $x \simeq \frac{Q^2}{W^2} \ll 1$  the virtual spacelike photon on the proton fluctuates are defined into on-shell quark-antiquark,  $q\bar{q}$ , vector state. Here  $Q^2$  refers to the photon virtuality and  $W$  to the photon-proton center-of-mass energy. In this process photon interact with the proton via coupling of two gluons to the  $q\bar{q}$  color dipole, where this called the color-dipole picture (CDP) of low- $x$  DIS [1-3]. The mass of  $q\bar{q}$  dipole, in terms of the transverse momentum  $\vec{k}_\perp$  is given by  $M_{q\bar{q}}^2 = \frac{k_\perp^2}{z(1-z)}$ , where  $\vec{k}_\perp$  is defined with respect to the photon direction and the variable  $z$  characterizes the distribution of the momenta between quark and antiquark. The lifetime of the  $q\bar{q}$  dipole is defined by  $\tau = \frac{W^2}{Q^2 + M_{q\bar{q}}^2} \gg \frac{1}{M_p}$ , which it is much longer than its typical interaction time with the target at small  $x$ . This condition not only restricts the kinematical range of the color dipole model to  $x \ll 1$  but also saturate the  $\gamma^*$ -proton cross section with  $x \leq 0.1$  [4-6].

HERA have been combined the neutral current (NC) interaction data for  $0.045 \leq Q^2 \leq 50,000 \text{ GeV}^2$  and  $6 \times 10^{-7} \leq x_{Bj} \leq 0.65$  at values of the inelasticity,  $y = Q^2/(sx_{Bj})$ , between 0.005 and 0.95 [7]. The highest center-of-mass energy in deep inelastic scattering of electrons on protons was  $\sqrt{s} \simeq 320 \text{ GeV}$ . HERA data collected from 1992 until 2015 are listed in Table I. The electron-proton center of mass energy at the LHeC ranges up to  $\sqrt{s} \simeq 1.3 \text{ TeV}$  which it is about 30 times the center of mass energy range of ep collisions at HERA. The high-luminosity LHC program would be uniquely complemented by the proposed Large Hadron electron Col-

lider (LHeC), where it is a high-energy lepton-proton and lepton-nucleus collider based at CERN [8-9]. The kinematic range in the  $(x, Q^2)$  plane of the LHeC for electron and positron neutral-current (NC) for the high energy  $E_p = 7 \text{ TeV}$  is  $5 \times 10^{-6} \leq x \leq 0.8$  and  $5 \leq Q^2 \leq 10^6 \text{ GeV}^2$  and  $5 \leq Q^2 \leq 5 \times 10^5 \text{ GeV}^2$  respectively. Today, an integrated Future Circular Collider programme consisting of a luminosity-frontier highest-energy lepton collider followed by an energy-frontier hadron collider is called FCC [10]. In this collider the FCC-eh with 50 TeV proton beams colliding with 60 GeV electrons from an energy-recovery linac would generate  $\sim 2 \text{ ab}^{-1}$  of 3.5 TeV ep collisions. The LHeC and FCC-eh lead into the region of high parton densities at small Bjorken  $x$ . Deep inelastic scattering measurements at FCC-eh and LHeC will allow the determination of the longitudinal structure function which its determination was so difficult at HERA [10].

The inclusive, deep inelastic electron-proton scattering cross section at low  $Q^2$  (i.e.  $Q^2 \ll M_Z^2$  which the contribution of Z exchange is negligible), can be written in its reduced form,

$$\begin{aligned} \sigma_r(x, Q^2) &= \frac{d^2\sigma}{dx dQ^2} \cdot \frac{Q^4 x}{2\pi\alpha^2 Y_+} \\ &= F_2(x, Q^2) \left[ 1 - \frac{y^2}{Y_+} \frac{F_L(x, Q^2)}{F_2(x, Q^2)} \right]. \end{aligned} \quad (1)$$

The reduced cross section is defined by two proton structure functions,  $F_2$  and  $F_L$  where  $Y_+ = 1 + (1 - y)^2$  and  $\alpha$  is the fine structure constant. At high- $y$  (very low  $x$ ) a characteristic bending of the reduced cross section is observed, which it is attributed to the contribution due to the longitudinal structure function.

The proton structure function  $F_2$  and the longitudinal structure function  $F_L$ , for a given Bjorken  $x$  and virtuality  $Q^2$ , can be written in terms of the  $\gamma^*p$  total cross

\*brezaei@razi.ac.ir

†Electronic address: grboroun@gmail.com; boroun@razi.ac.ir

section as follows,

$$\begin{aligned} F_2(x, Q^2) &= \frac{Q^2}{4\pi^2\alpha} [\sigma_L^{\gamma^*p}(x, Q^2) + \sigma_T^{\gamma^*p}(x, Q^2)], \\ F_L(x, Q^2) &= \frac{Q^2}{4\pi^2\alpha} \sigma_L^{\gamma^*p}(x, Q^2). \end{aligned} \quad (2)$$

The subscript  $L$  and  $T$  referring to the transverse and longitudinal polarization state of the exchanged boson. The ratio of the longitudinal to transverse cross sections is termed

$$R(x, Q^2) = \frac{\sigma_L(x, Q^2)}{\sigma_T(x, Q^2)} = \frac{F_L}{F_2 - F_L}. \quad (3)$$

In the dipole picture, the total deep inelastic cross-section can be factorized in the following form

$$\begin{aligned} \sigma_{L,T}^{\gamma^*p}(x, Q^2) &= \int dz d^2\mathbf{r}_\perp |\Psi_\gamma^{L,T}(\mathbf{r}_\perp, z(1-z), Q^2)|^2 \\ &\times \sigma_{q\bar{q}}(\mathbf{r}_\perp, z(1-z), W^2), \end{aligned} \quad (4)$$

where  $\Psi_\gamma^{L,T}$  are the appropriate spin averaged light-cone wave functions of the photon and  $\sigma_{q\bar{q}}(r, z, W^2)$  is the dipole cross-section which related to the imaginary part of the  $(q\bar{q})p$  forward scattering amplitude. The variable  $z$ , with  $0 \leq z \leq 1$ , characterizes the distribution of the momenta between quark and antiquark. The square of the photon wave function describes the probability for the occurrence of a  $(q\bar{q})$  fluctuation of transverse size with respect to the photon polarization [3-6,11].

The ratio of the structure functions is related to the longitudinal-to-transverse ratio of the photo absorption cross sections as is given by

$$\frac{F_L(x, Q^2)}{F_2(x, Q^2)} = \frac{R(x, Q^2)}{1 + R(x, Q^2)}. \quad (5)$$

In Refs.[1-5], authors show that at large  $Q^2 \gg \Lambda_{sat}^2(W^2)$ , the ratio of the photo absorption cross sections is given by the theoretically preferred value of  $\rho$  as

$$\begin{aligned} R(W^2, Q^2)|_{Q^2 \gg \Lambda_{sat}^2(W^2)} &= \frac{1}{2\rho}, \\ \text{where } \rho_W = \rho &= \frac{4}{3}. \end{aligned} \quad (6)$$

The structure function  $F_2(x, Q^2)$  presented in terms of the color-dipole cross section [1] as the leading contribution defined by

$$\begin{aligned} F_2(x, Q^2) &= \frac{Q^2}{4\pi^2\alpha} \sigma^{\gamma^*p}(W^2, Q^2) = \frac{Q^2}{4\pi^2\alpha} (\sigma_L^{\gamma^*p}(W^2, Q^2) \\ &+ \sigma_T^{\gamma^*p}(W^2, Q^2)), \end{aligned} \quad (7)$$

which at large- $Q^2$  limit becomes [2]

$$F_2(x, Q^2) = \frac{R_{e^+e^+}}{36\pi^2} (T(W^2) + \frac{1}{2}L(W^2)), \quad (8)$$

where  $R_{e^+e^+} = 10/3$  for even active flavor number. After some assumptions about the sea-quark and gluon distribution behavior into the kinematic variable  $W^2$  one obtained that [1-2]

$$T(W^2) = \rho L(W^2), \quad (9)$$

which  $F_2$  in (8) becomes

$$F_2(x, Q^2) = \frac{R_{e^+e^+}}{36\pi^2} T(W^2) (1 + \frac{1}{2\rho}). \quad (10)$$

Indeed the longitudinal-to-transverse ratio of the photoabsorption cross sections is related to  $\rho \equiv \rho(x, Q^2)$  as

$$R(x, Q^2) = \frac{\sigma_L^{\gamma^*p}(W^2, Q^2)}{\sigma_T^{\gamma^*p}(W^2, Q^2)} = \frac{1}{2\rho(x, Q^2)}. \quad (11)$$

In terms of  $\rho$  the ratio of structure functions becomes

$$\frac{F_L(x, Q^2)}{F_2(x, Q^2)} = \frac{1}{1 + 2\rho(x, Q^2)}. \quad (12)$$

The factor 2 originates from the difference in the transverse and longitudinal photon wave function and the factor  $\rho$  is associated with different interaction of photons into  $q\bar{q}$  pairs,  $\gamma_{L,T}^* \rightarrow q\bar{q}$ . The value of  $\rho$  predicted to be 1 in Ref.[1] or  $\frac{4}{3}$  in Ref.[2-3]. Authors in Ref.[1] show that those previous fit to the experimental data was based on  $\rho = 1$  which defined the equality of

$$\bar{\sigma}_{(q\bar{q})_T}^{J=1}(\vec{l}_\perp'^2, W^2) = \bar{\sigma}_{(q\bar{q})_L}^{J=1}(\vec{l}_\perp'^2, W^2), \quad (13)$$

where they are related to the color-dipole cross section with respect to the gauge-theory structure as

$$\sigma_{(q\bar{q})_p}(\vec{r}_\perp, W^2) = \int d^2l_\perp \bar{\sigma}_{(q\bar{q})_p}(\vec{l}_\perp^2, W^2) (1 - e^{-i\vec{l}_\perp \cdot \vec{r}_\perp}). \quad (14)$$

Indeed, helicity independence (i.e.,  $\rho = 1$ ) leads to  $R(W^2, Q^2) = 0.5$  and one obtains  $F_L(W^2, Q^2)/F_2(W^2, Q^2) = 1/3 = 0.333$ . Also, authors in Refs.[2-3] connected the  $q\bar{q}$ -proton interaction with introducing a proportionality factor  $\rho$  as

$$\bar{\sigma}_{(q\bar{q})_T}^{J=1}(\vec{l}_\perp'^2, W^2) = \rho \bar{\sigma}_{(q\bar{q})_L}^{J=1}(\vec{l}_\perp'^2, W^2). \quad (15)$$

The mass  $M_{q\bar{q}}$  (in terms of the transverse momentum  $\vec{k}_\perp$ ) with respect to the photon direction is given by

$$M_{q\bar{q}}^2 = \frac{\vec{k}_\perp^2}{z(1-z)}. \quad (16)$$

The average transverse momenta squared with respect to the longitudinal and transverse photons is defined by the following forms

$$\langle \vec{k}_\perp^2 \rangle_{L,T} = M_{q\bar{q}}^2 \int_0^1 dz z(1-z) f_{L,T}(z), \quad (17)$$

where

$$f_L(z) = 6z(1-z) \quad (18)$$

and

$$f_T(z) = \frac{3}{2}(1-2z(1-z)). \quad (19)$$

Explicitly one obtained from Ref.[2-3]

$$\rho = \frac{\langle \vec{k}_\perp^2 \rangle_L}{\langle \vec{k}_\perp^2 \rangle_T} = \frac{4}{3}, \quad (20)$$

which shows  $R(W^2, Q^2) = 3/8 = 0.375$  and in terms of structure functions  $F_L(W^2, Q^2)/F_2(W^2, Q^2) = 3/11 = 0.273$ .

These results are corresponding to the helicity fluctuations of the photon on the proton. Our insight into the dynamics of the these fluctuations might determined  $\rho(x, Q^2)$  in comparison with the measurement data and provides some constraints on the CDP bounds.

To investigate the role of the CDP on the ratio  $F_L/F_2$  at low  $x$  region, we first determine this behavior using the known  $F_2$  parameterization [12] and the DGLAP evolution equations [13]. Then the color-dipole cross sections should be driven by the power-law behavior of the exponents. Besides hard pomeron behavior for the exponents in the low  $x$  region, the singlet effective exponent is expected to modify the behavior of the ratio  $F_L/F_2$ . Then the nonlinear corrections at low  $Q^2$  values controlled the ratio behavior in contrast to the CDP bounds.

### Method

At small  $x$  which the gluon density is dominant, the linear DGLAP  $Q^2$  evolution equations may eventually have to be replaced by a BFKL [14] type of law. In this theoretical framework, the gluon density is defined on the basis of  $F_2$  and  $F_L$  which it is a test higher order QCD at small  $x$ . Through the measurement of the  $Q^2$  dependence of  $F_2$  in DIS the gluon density can be determined. The relation between the gluon distribution and the proton structure function is prescribed [15-16] by the DGLAP evolution equation in the following form

$$G(x, Q^2) = \frac{1}{\Theta_{qg}(x, Q^2)} \left[ \frac{\partial F_2(x, Q^2)}{\partial \ln Q^2} - \Phi_{qg}(x, Q^2) F_2(x, Q^2) \right], \quad (21)$$

where the parameterization  $F_2(x, Q^2)$  and its derivatives suggested in Ref.[12]. The kernels for the quark and gluon sectors (denoted by  $\Phi$  and  $\Theta$ ) presented by the following forms

$$\begin{aligned} \Theta_{qg}(x, Q^2) &= P_{qg}(x, \alpha_s) \otimes x^{\lambda_g}, \\ \Phi_{qg}(x, Q^2) &= P_{qg}(x, \alpha_s) \otimes x^{\lambda_s}, \end{aligned} \quad (22)$$

where the splitting functions expanded into one, two and three loops correction in Ref.[17]. The exponents  $\lambda_s$  and  $\lambda_g$  are defined by the derivatives of the distribution functions by the following forms as  $\lambda_s = \partial \ln F_2^s(x, Q^2) / \partial \ln(1/x)$  and  $\lambda_g = \partial \ln G(x, Q^2) / \partial \ln(1/x)$ . The running coupling constant  $\alpha_s$  has the following forms in NNLO analysis

$$\alpha_s^{\text{NNLO}} = \frac{4\pi}{\beta_0 t} \left[ 1 - \frac{\beta_1 \ln t}{\beta_0^2 t} + \frac{1}{(\beta_0 t)^2} \left[ \left( \frac{\beta_1}{\beta_0} \right)^2 (\ln^2 t - \ln t + 1) + \frac{\beta_2}{\beta_0} \right] \right], \quad (23)$$

where  $\beta_0 = \frac{1}{3}(33 - 2n_f)$ ,  $\beta_1 = 102 - \frac{38}{3}n_f$  and  $\beta_2 = \frac{2857}{6} - \frac{6673}{18}n_f + \frac{325}{54}n_f^2$ . The variable  $t$  is defined as  $t = \ln(\frac{Q^2}{\Lambda^2})$  and  $\Lambda$  is the QCD cut-off parameter for each heavy quark mass threshold as we take the  $n_f = 4$  for  $m_c^2 < \mu^2 < m_b^2$ .

On the other hand, the longitudinal structure function is directly sensitive to the gluon density. Beyond the parton model the  $F_L$  effects can be sizable, hence it can not be longer neglected. Also, the longitudinal structure function is predominant in cosmic neutrino-hadron cross section scattering. This behavior for the longitudinal structure function will be checked in high energy process such as the Large Hadron electron Collider (LHeC) project which runs to beyond a TeV in center-of-mass energy [8-10]. The final measurement of  $F_L$  at HERA was determined in Ref.[18]. HERA collected  $ep$  collision data with the H1 detector at a electron beam energy of 27.6 GeV and proton beam energies of 920, 575 and 460 GeV, which allowed a measurement of structure functions at  $x$  values  $6.5 \times 10^{-4} \leq x \leq 0.65$  and  $Q^2$  values  $35 \text{ GeV}^2 \leq Q^2 \leq 800 \text{ GeV}^2$ . The variation in inelasticity  $y$  was achieved at HERA by comparing high statistics data at highest energy,  $E_p = 920 \text{ GeV}$ , with about  $13 \text{ pb}^{-1}$  of data at 460 GeV and  $7 \text{ pb}^{-1}$  at 575 GeV.

In perturbative QCD, the longitudinal structure function in terms of the coefficient functions at small  $x$  is given by

$$x^{-1} F_L = \langle e^2 \rangle (C_{L,q} \otimes q_s + C_{L,g} \otimes g). \quad (24)$$

Here  $\langle e^k \rangle$  is the average of the charge  $e^k$  for the active quark flavors,  $\langle e^k \rangle = n_f^{-1} \sum_{i=1}^{n_f} e_i^k$ . The perturbative expansion of the coefficient functions can be written as [19]

$$C_{L,a}(\alpha_s, x) = \sum_{n=1} a(t)^n c_{L,a}^n(x), \quad (25)$$

where  $n$  is the order in the running coupling constant. The running coupling constant in the high-loop corrections of the above equation is expressed entirely thorough the variable  $a(t)$ , as  $a(t) = \frac{\alpha_s}{4\pi}$ . The explicit expression for the coefficient functions in LO up to NNLO are presented in Refs.[20-21].

Therefore the longitudinal structure function is given by the similar method in Ref.[22] as

$$F_L(x, Q^2) = F_2(x, Q^2)I_{L,q}(x, Q^2) + G(x, Q^2)I_{L,g}(x, Q^2). \quad (26)$$

One can rewrite the gluon distribution with respect to the proton structure function  $F_2(x, Q^2)$  and its derivative  $\partial F_2(x, Q^2)/\partial \ln Q^2$  (i.e., Eq.21), then we will have

$$F_L(x, Q^2) = \frac{I_{L,g}(x, Q^2)}{\Theta_{qg}(x, Q^2)} \frac{\partial F_2(x, Q^2)}{\partial \ln Q^2} + \{I_{L,q}(x, Q^2) - \Phi_{qq}(x, Q^2) \frac{I_{L,g}(x, Q^2)}{\Theta_{qg}(x, Q^2)}\} F_2(x, Q^2), \quad (27)$$

where the analytical results for the compact form of the kernels ( $\Phi$ ,  $\Theta$  and  $I$ ) at LO are given in Appendix A.

The ratio of the proton structure functions takes the form

$$\frac{F_L(x, Q^2)}{F_2(x, Q^2)} = \eta(x, Q^2) + \zeta(x, Q^2) \frac{\partial \ln F_2(x, Q^2)}{\partial \ln Q^2}, \quad (28)$$

where

$$\begin{aligned} \eta(x, Q^2) &= I_{L,q}(x, Q^2) - \Phi_{qq}(x, Q^2) \frac{I_{L,g}(x, Q^2)}{\Theta_{qg}(x, Q^2)}, \\ \zeta(x, Q^2) &= \frac{I_{L,g}(x, Q^2)}{\Theta_{qg}(x, Q^2)}. \end{aligned} \quad (29)$$

Consequently, one can obtain the ratio  $F_L/F_2$  from the parameterization of  $F_2$ . In Ref.[12] suggested a new parametrization which describes fairly well the available experimental data on the reduced cross sections in an agreement with the Froissart predictions. Also a theoretical analysis investigated the behavior of the longitudinal structure function at small  $x$  by employing the parametrization of  $F_2$  presented in Ref.[23].

The explicit expression for the  $F_2$  parameterization [12], which obtained from a combined fit of the H1 and ZEUS collaborations data [24] in a range of the kinematical variables  $x$  and  $Q^2$  ( $x < 0.01$  and  $0.15 < Q^2 < 3000 \text{ GeV}^2$ ), reads as

$$F_2^{\gamma p}(x, Q^2) = D(Q^2)(1-x)^n \sum_{m=0}^2 A_m(Q^2) L^m, \quad (30)$$

where

$$\begin{aligned} A_0(Q^2) &= a_{00} + a_{01} \ln(1 + \frac{Q^2}{\mu^2}), \\ A_1(Q^2) &= a_{10} + a_{11} \ln(1 + \frac{Q^2}{\mu^2}) + a_{12} \ln^2(1 + \frac{Q^2}{\mu^2}) Q^2, \\ A_2(Q^2) &= a_{20} + a_{21} \ln(1 + \frac{Q^2}{\mu^2}) + a_{22} \ln^2(1 + \frac{Q^2}{\mu^2}) Q^2, \\ D(Q^2) &= \frac{Q^2(Q^2 + \lambda M^2)}{(Q^2 + M^2)^2}, \\ L^m &= \ln^m(\frac{1}{x} \frac{Q^2}{Q^2 + \mu^2}). \end{aligned} \quad (31)$$

Here  $M$  is the effective mass and  $\mu^2$  is a scale factor. The additional parameters with their statistical errors are given in Table II.

Therefore with respect to the parameterization of  $F_2$  the final result for the ratio  $F_L/F_2$  is

$$\begin{aligned} \frac{F_L(x, Q^2)}{F_2(x, Q^2)} &= \eta(x, Q^2) + \zeta(x, Q^2) \left\{ \frac{\partial \ln D(Q^2)}{\partial \ln Q^2} \right. \\ &\quad \left. + \frac{\partial \ln(\sum_{m=0}^2 A_m(Q^2) L^m)}{\partial \ln Q^2} \right\}. \end{aligned} \quad (32)$$

At last, the ratio of the longitudinal to transverse cross sections is termed

$$R(x, Q^2) = Eq.(32)/(1 - Eq.(32)). \quad (33)$$

At small  $x \leq Q^2/W^2 \ll 1$  and sufficiently large  $Q^2$  the deep inelastic scattering is recognized as elastic diffractive forward scattering of  $(q\bar{q})_{L,T}^{J=1}$  fluctuations of the photon on the proton [1-5]. Therefore in CDP the proton structure function defined by the single variable  $W^2$  as

$$F_2(x, Q^2) = F_2(W^2 = \frac{Q^2}{x}). \quad (34)$$

Exploiting a power-law dependence for  $F_2(W^2)$  on  $W^2$  by the following form

$$F_2(W^2) \sim (W^2)^{\lambda_s} = (\frac{Q^2}{x})^{\lambda_s}, \quad (35)$$

where the exponent  $\lambda_s$  is defined

$$\lambda_s = \frac{\partial \ln F_2(W^2)}{\partial \ln W^2}. \quad (36)$$

Substitution of (36) into (28) implies the interesting relation for the ratio  $F_L/F_2$  as

$$\frac{F_L(W^2)}{F_2(W^2)} = \eta(W^2) + \zeta(W^2) \lambda_s|_x. \quad (37)$$

Equivalently, the ratio of structure functions in terms of  $\rho_w$  is obtained by the following form

$$\frac{1}{1 + 2\rho_w} = \eta(W^2) + \zeta(W^2) \lambda_s, \quad (38)$$

where

$$\rho_w = \frac{1 - \eta(W^2) - \zeta(W^2) \lambda_s}{2(\eta(W^2) + \zeta(W^2) \lambda_s)}, \quad (39)$$

or

$$R_w = \frac{\eta(W^2) + \zeta(W^2) \lambda_s}{1 - \eta(W^2) - \zeta(W^2) \lambda_s}. \quad (40)$$

## Results and Discussion

To study the effects of  $F_2$  parameterization and of singlet exponent in the ratio  $F_L/F_2$  at low  $x$  at NNLO analysis we compare the ratio in HERA range with those using a strick bound for this ratio. We use the  $F_2$  parameterization [12] where fitted to the combined H1 and ZEUS inclusive DIS data [24] in a range of the kinematical variables  $x < 0.01$  and  $0.15 \text{ GeV}^2 < Q^2 < 3000 \text{ GeV}^2$ . The coupling constant defined via the  $n_f = 4$  definition of  $\Lambda_{QCD}$  for the ZEUS data [24] and the MRST set of partons [26]. The values of  $\Lambda_{QCD}$  at LO upto NNLO are displayed in Table III respectively. The values of  $\lambda_s \simeq 0.33$  and  $\lambda_g \simeq 0.43$  are used within the range of  $Q^2$  under study [27-28, 25, 29]. The predictions for the ratio of the structure functions, in the HERA kinematic range [18], are computed and compared at low values of  $x$ . The results have been depicted at fixed value of the invariant mass  $W$  (i.e.  $W = 230 \text{ GeV}$ ).

Some analytical solutions have been shown that in the dipole model there is a strict bound that  $\frac{F_L(x, Q^2)}{F_2(x, Q^2)} < 0.27$  [30-31]. In realistic dipole-proton cross section authors in Ref.[32] shown that the bound is lower than 0.27 with the ratio  $\simeq 0.22$ . These results have been reported in Refs.[1-5] with considerable different between the fluctuations of interaction  $q\bar{q}$  where originated from the photon polarizations. The ratio of the structure functions in CDP depends on the interpretation of  $\rho_w$  as defined in Eqs.(13) and (15).

The results, with respect to Eq.(32), are presented in Fig.1 and compared with the H1 data [18] as accompanied with total errors. As can be seen in this figure, the depletion and enhancement in this ratio reflect the experimental data and it is comparable with the H1 data in the interval  $1 \text{ GeV}^2 < Q^2 < 500 \text{ GeV}^2$ . The error bares are according to the statistical errors of the  $F_2$  parameterization in accordance with Table II. A detailed comparison has also been shown with the CDP bounds and depicted in Fig.1. We note that the ratio of the structure functions are rather close to the upper bounds especially for  $1 < Q^2 \leq 20 \text{ GeV}^2$  at fixed value of the invariant mass. The  $R$  ratio is expected to vanish at large  $Q^2$  and moderate  $x$  in the naive parton model, but it is nonzero at low values of  $x$ . It dues to the fact that partons can carry transverse momentum [33]. In Fig.(2) we present the ratio  $R$ , with respect to Eq.(33), in comparison with the H1 data using the  $F_2$  parameterization. As can be seen in this figure, one can conclude that the these results essentially improve the good agreement with data in comparison with the CDP bounds at the wide range of  $Q^2$  values. In Ref.[34] the ratio  $R$  is found at  $R = 0.260 \pm 0.050$  which this value is constant at the region  $7.10^{-5} < x < 2.10^{-3}$  and  $3.5 \leq Q^2 \leq 45 \text{ GeV}^2$ . In color dipole model the ratio  $R$  lead to the bound  $R \leq 0.372$  [31,35]. In Ref.[36] ZEUS collaboration is shown that the overall

value of  $R$  from both the unconstrained and constrained fits is  $R = 0.105^{+0.055}_{-0.037}$  in a wide range of  $Q^2$  values ( $5 \leq Q^2 \leq 110 \text{ GeV}^2$ ). Therefore, this ratio (i.e., Fig.2) is comparable with those obtained in literature at some fixed point, but in a wide range of  $Q^2$  values it is compatible with the experimental data.

To emphasize the size of the CDP bound, we show that the ratio  $F_L/F_2$  and  $R$  have a maximum behavior when the proton structure function has a power law behavior. In Eqs.(37) and (40) a power law in  $F_2$  with  $\lambda = \text{const.}$  occurs in Regge phenomenology behavior. The gluon exponent has been fixed at a hard pomeron value as  $\lambda_g$  is comparable with the so-called hard pomeron intercept. The exponent for gluon distribution is defined with a value of  $\lambda_g = 0.424$  which it is the hard pomeron part of Regge phenomenology [37]. We choice that the singlet exponent value is consistent with the experimental data and CDP bound if one definite value  $0.27 \leq \lambda_s \leq 0.33$  [1-5, 15-16, 37]. In Figs.(3) and (4) the ratio  $F_L/F_2$  and  $R$  based on the gluon and singlet exponents have been presented at  $W = 230 \text{ GeV}$ . These behaviors are in good agreements with the ones obtained by the CDP bound when applying the uncertainty principle. These results indicate a decrease of the ratios for small  $Q^2$  which it is require with respect to the electromagnetic gauge invariance. On the other hand, at large  $Q^2$  values the exponent method (i.e., Eqs.(32) and (33)) is not consistent with the experimental data when compared with the  $F_2$  parameterization method (i.e., Eqs.(37) and (40)).

The strong rise into the  $k_T$  factorization formula is also true for the singlet structure function. This behavior coming from resummation of large powers of  $\alpha_s \ln 1/x$  where its achieved by the use of the  $k_T$  factorization formalism. The small- $x$  resummation requires an all-order class of subleading corrections in order to lead to stable results [38]. However the effective pomeron is  $Q^2$ -dependent when structure functions fitted to the experimental data at low values of  $x$ . Here, we take into account the effects of kinematics which lead to a shift from the pomeron exponent to the effective exponent.

To better illustrate our calculations at all  $Q^2$  values, we used effective exponent in the form of  $\lambda(Q^2)$ . The obtained results based on  $\lambda(Q^2)$  are presented based on H1 and H1-ZEUS combined data for the proton structure functions at  $4 < Q^2 < 200 \text{ GeV}^2$ . In Ref.[39], an eyeball fit was given by the following form

$$\lambda_{eff}(Q^2) = 0.13 + 0.1 \left(\frac{Q^2}{10}\right)^{0.35}. \quad (41)$$

Also authors in Ref.[40] have derived the phenomenological exponent of singlet density for combined HERA  $e^+p$  DIS data [41] within the saturation model where  $\lambda_{phn}(Q^2)$  can be parameterized as

$$\lambda_{phn}(Q^2) = 0.329 + 0.1 \log\left(\frac{Q^2}{90}\right). \quad (42)$$

In Figs.(5) and (6) we plot ratios  $F_L/F_2$  and  $R$  for  $\lambda(Q^2)$  and compatible with the CDP bounds. A comparison with HERA data at fixed invariant mass have also been shown there. The results for these ratios have been presented as a function of  $Q^2$  at  $W = 230$  GeV. It is seen that our results based on the power-law behavior at NNLO approximation over a wide range of  $x$  and  $Q^2$  values are comparable with the experimental data at low and moderate  $Q^2$  values. At high- $Q^2$  values we observed an overall shift between the HERA data and the predictions. This behavior can be resolved with an adjustment of singlet exponent than one obtained with respect to the effective and phenomenological exponents in Eqs.(41) and (42) respectively.

The agreement between the method and the experimental data is good until  $Q^2 = 200$  GeV<sup>2</sup> as  $\lambda(Q^2)$  reported in Eqs.(41) and (42) parameterized for  $Q^2 < 200$  GeV<sup>2</sup>. One can conclude that exponent defined for singlet distribution is larger than the gluon exponent at large  $Q^2$  values where this behavior is not consistent with pQCD.

### Nonlinear Correction to the $F_2$ parameterization

In figures (1) and (2) we observed that the behavior of ratios can be corrected when the nonlinear correction is taken account. The nonlinear effects are provided by a multiple gluon interaction which leads to the nonlinear terms in the derivation of the linear DGLAP evolution equations. Therefore the standard linear DGLAP evolution equations will be modified by the nonlinear corrections. Indeed the origin of the shadowing correction, in pQCD interactions, is primarily considered as the gluon recombination ( $g + g \rightarrow g$ ) which is simply the inverse process of gluon splitting ( $g \rightarrow g + g$ ).

Gribov, Levin, Ryskin, Mueller and Qiu (GLR-MQ) [42] performed a detailed study of these recombination processes. This widely known as the GLR-MQ equation and involves the two-gluon distribution per unit area of the hadron. This equation predicts a saturation behavior of the gluon distribution at very small  $x$  [43-45]. A closer examination of the small  $x$  scattering is resummation powers of  $\alpha_s \ln(1/x)$  where leads to the  $k_T$ -factorization form [46]. In the  $k_T$ -factorization approach the large logarithms  $\ln(1/x)$  are relevant for the unintegrated gluon density in a nonlinear equation. Solution of this equation develops a saturation scale where tame the gluon density behavior at low values of  $x$  and this is an intrinsic characteristic of a dense gluon system.

Therefore one should consider the low-  $x$  behavior of the singlet distribution using the nonlinear GLR-MQ evolution equation. The shadowing correction to the evolution

of the singlet quark distribution can be written as [47]

$$\frac{\partial xq(x, Q^2)}{\partial \ln Q^2} = \frac{\partial xq(x, Q^2)}{\partial \ln Q^2} \Big|_{DGLAP} - \frac{27\alpha_s^2}{160R^2Q^2} [xg(x, Q^2)]^2. \quad (43)$$

Eq. (43) can be rewrite in a convenient form as

$$\frac{\partial F_2(x, Q^2)}{\partial \ln Q^2} = \frac{\partial F_2(x, Q^2)}{\partial \ln Q^2} \Big|_{DGLAP} - \frac{5}{18} \frac{27\alpha_s^2}{160R^2Q^2} \times [xg(x, Q^2)]^2. \quad (44)$$

The first term is the standard DGLAP evolution equation and the value of  $R$  is the correlation radius between two interacting gluons. It will be of the order of the proton radius ( $R \simeq 5$  GeV<sup>-1</sup>), if the gluons are distributed through the whole of proton, or much smaller ( $R \simeq 2$  GeV<sup>-1</sup>) if gluons are concentrated in hot-spot within the proton.

Also there is another mechanism to prevent generation of the high density gluon states, as this is well known the vacuum color screening [48]. There is a transition between the nonperturbative and perturbative domains. In the QCD vacuum, the non-perturbative fields form structures with sizes  $\sim R_c$  which it is smaller than  $\Lambda_{QCD}$ . The short propagation length for perturbative gluons is  $R_c \sim 0.2 - 0.3$  fm. The gluon fusion effect in non-linear regime controlled by the new dimensionless parameter  $\sim \frac{R_c^2}{8B}$  where  $B$  is the characteristic size of the interaction region as this parameter can be defined by  $\ln(x_0/x)$  and  $r$  where  $r^2 \sim Q^{-2}$ . Authors in this reference (i.e., Ref.[48]) show that the nonlinear effects lead to the logarithmically ratio as the nonlinear/linear effects are proportional to  $R_c^2/8B(\ln(x_0/x), r^2) \ln(Q^2 R_c^2)$ .

Combining Eqs. (21) and (44), one can consider the nonlinear correction to the gluon distribution function as

$$G(x, Q^2) = \frac{1}{\Theta_{qq}(x, Q^2)} \left[ \frac{\partial F_2(x, Q^2)}{\partial \ln Q^2} - \frac{5}{18} \frac{27\alpha_s^2}{160R^2Q^2} \times G^2(x, Q^2) - \Phi_{qq}(x, Q^2) F_2(x, Q^2) \right], \quad (45)$$

where

$$G(x, Q^2) + \frac{1}{\Theta_{qq}(x, Q^2)} \frac{5}{18} \frac{27\alpha_s^2}{160R^2Q^2} G^2(x, Q^2) = \frac{1}{\Theta_{qq}(x, Q^2)} \left[ \frac{\partial F_2(x, Q^2)}{\partial \ln Q^2} - \Phi_{qq}(x, Q^2) F_2(x, Q^2) \right]. \quad (46)$$

Eq.(46) is a second-order equation which can be solved as

$$\begin{aligned}
G(x, Q^2) &= G(x, Q^2) \left[ 1 - \frac{\mathcal{A}(x, Q^2)}{\Theta_{qg}(x, Q^2)} G(x, Q^2) \right. \\
&\quad + 2 \left( \frac{\mathcal{A}(x, Q^2)}{\Theta_{qg}(x, Q^2)} G(x, Q^2) \right)^2 \\
&\quad \left. - 5 \left( \frac{\mathcal{A}(x, Q^2)}{\Theta_{qg}(x, Q^2)} G(x, Q^2) \right)^3 + \dots \right] \\
&= G(x, Q^2) [1 - \mathcal{N} + 2\mathcal{N}^2 - 5\mathcal{N}^3 + \dots] \\
&= G(x, Q^2) [\mathcal{N}\mathcal{L}\mathcal{C}], \tag{47}
\end{aligned}$$

where  $\mathcal{N} = \frac{\mathcal{A}(x, Q^2)}{\Theta_{qg}(x, Q^2)} G(x, Q^2)$  and  $\mathcal{A}(x, Q^2) = \frac{5}{18} \frac{27\alpha_s^2}{160R^2Q^2}$ . Therefore the nonlinear corrections ( $\mathcal{N}\mathcal{L}\mathcal{C}$ s) to the ratio  $F_L/F_2$  are obtained by the following form as

$$\begin{aligned}
\frac{F_L(x, Q^2)}{F_2(x, Q^2)}|_{\text{Nonlinear}} &= I_{L,q}(x, Q^2) + \frac{I_{L,g}(x, Q^2)}{\Theta_{qg}(x, Q^2)} \\
&\quad \times \left\{ \left( \frac{\partial \ln D(Q^2)}{\partial \ln Q^2} + \frac{\partial \ln(\sum_{m=0}^2 A_m(Q^2) L^m)}{\partial \ln Q^2} \right) \right. \\
&\quad \left. - \Phi_{qq}(x, Q^2) \right\} [\mathcal{N}\mathcal{L}\mathcal{C}]. \tag{48}
\end{aligned}$$

Also, the nonlinear correction to the ratio of the longitudinal to transverse cross sections is defined

$$R(x, Q^2)|_{\text{Nonlinear}} = Eq.(48)/(1 - Eq.(48)). \tag{49}$$

The nonlinear corrections (NLCs) to the ratio of  $F_L/F_2$  and  $R$  are considered in a wide range of  $Q^2$  values at a fixed value of the invariant mass in Fig.7. In this figure (i.e., Fig.7), the effects of nonlinearity are investigated for  $R = 2 \text{ GeV}^{-1}$  in comparison with the linear behavior from the  $F_2$  parameterization. One can see that obtained nonlinear corrections for these ratios are observable at low  $Q^2$  values ( $1 < Q^2 < 10 \text{ GeV}^2$ ) and are comparable with the H1 data in a wide range of  $Q^2$  values when we compare with the CDP bounds. On the other hand, these nonlinear behaviors have been shown for both of the ratios with respect to the effective exponent  $\lambda(Q^2)$  in figure 8. The error bands represent the uncertainty estimation coming from the  $F_2$  parameterization. As one can see in this plot, the inclusion of the nonlinear behavior by the effective exponent, significantly change the behavior of the ratio of  $F_L/F_2$  and  $R$ . One can see an enhancement for the moderate value of  $Q^2$  and reduction for the small and large values of  $Q^2$ . The results for the ratios clearly show significant agreement over a wide range of  $x$  and  $Q^2$  variables. The comparison of the results reveals the following conclusion: For a fixed value of the invariant mass  $W$ , one see the same patterns for the ratios when the effective exponent is  $Q^2$ -dependent. They show a pick around the moderate value of  $Q^2$ ,  $Q^2 \sim 5 \text{ GeV}^2$ . One of the main important results can be concluded from this figure is the significant reduction in ratio

of  $F_L/F_2$  and  $R$  at low  $Q^2$  values due to including nonlinear effects with respect to the effective exponent in the analysis.

## Conclusion

In conclusion, we presented the high-order corrections to the ratio  $F_L/F_2$  and  $R$  with respect to the derivative of the proton structure function into  $\ln(Q^2)$ . In this paper we have used different variants of the proton structure function. Firstly the ratios determined in the kinematical region range where  $F_2$  has been parameterized. The behavior of ratios in comparison with the experimental data are in good agreement in a wide range of  $Q^2$  values at a fixed invariant mass. Therefore the obtained ratios are different than the ones of CDP bounds. Only at low  $Q^2$  values the ratios are close to the bounds. In this region, we have studied the effects of adding the nonlinear corrections to the ratio  $F_L/F_2$  and  $R$ . These corrections are close to the data for low- $Q^2$  values as we have discussed the meaning of this finding from the point of view of modified nonlinear behavior of the ratios. Secondly the power-law behavior for the proton structure function is predicted. The results for a fixed exponent is close to the bounds in CDP and are comparable with the experimental data at moderate  $Q^2$  values. At low and moderate  $Q^2$  values an effective exponent should be considered.

Therefore the predictions of  $F_L/F_2$  and  $R$  with respect to the  $F_2$  parameterization give very valuable information on the programs for future electron- and positron-proton scattering experiments such as LHeC and FCC-eh at a wide range of  $Q^2$  values. This analysis is also enriched with the nonlinear contributions to the ratios with respect to the effective exponent. It has been clearly demonstrated in our analysis that the nonlinear contribution by the effective exponent is required for the low values of  $Q^2$ .

## ACKNOWLEDGMENTS

Authors are grateful the Razi University for financial support of this project and also G.R.Boroun is thankful the CERN theory department for their hospitality and support during the preparation of this paper.

## Appendix A

The kernels presented for the quark and gluon sectors, denoted by  $\Phi$  and  $\Theta$  respectively at LO up to NNLO,

$$\begin{aligned}\Theta_{qq}(x, Q^2) &= P_{qq}(x, \alpha_s) \otimes x^{\lambda_g}, \\ \Phi_{qq}(x, Q^2) &= P_{qq}(x, \alpha_s) \otimes x^{\lambda_s},\end{aligned}\quad (50)$$

have the following form at the leading order approximation as:

$$\begin{aligned}\Phi_{qq}(x, Q^2) &= \frac{\alpha_s}{4\pi} \left\{ 4 + \frac{16}{3} \ln\left(\frac{1-x}{x}\right) + \frac{16}{3} \int_x^1 \frac{z^{\lambda_s} - z^{-1}}{1-z} dz \right. \\ &\quad \left. - \frac{8}{3} \int_x^1 (1+z) z^{\lambda_s} dz \right\}, \\ \Theta_{qq}(x, Q^2) &= \frac{\alpha_s}{4\pi} \frac{20}{9} \int_x^1 (z^2 + (1-z)^2) z^{\lambda_g} dz.\end{aligned}\quad (51)$$

Also the longitudinal kernels at low- $x$  limit presented by the following forms

$$\begin{aligned}I_{L,q}(x, Q^2) &= C_{L,q}(x, \alpha_s) \otimes x^{\lambda_s}, \\ I_{L,g}(x, Q^2) &= C_{L,g}(x, \alpha_s) \otimes x^{\lambda_g}.\end{aligned}\quad (52)$$

can be defined at leading order approximation by:

$$\begin{aligned}I_{L,q}(x, Q^2) &= \frac{\alpha_s}{4\pi} \int_x^1 8n_f(1-z) z^{\lambda_s+1} dz, \\ I_{L,g}(x, Q^2) &= \frac{\alpha_s}{4\pi} \int_x^1 4C_F z^{\lambda_g+1} dz.\end{aligned}\quad (53)$$

TABLE I: HERA data collected by two collaborations H1 and ZEUS.

HERA	$e^+p$	$e^-p$
HERA I	100 pb $^{-1}$	15 pb $^{-1}$
HERA II	150 pb $^{-1}$	235 pb $^{-1}$

TABLE II: The effective Parameters at low  $x$  for  $0.15 \text{ GeV}^2 < Q^2 < 3000 \text{ GeV}^2$  provided by the following values. The fixed parameters are defined by the Block-Halzen fit to the real photon-proton cross section as  $M^2 = 0.753 \pm 0.068 \text{ GeV}^2$  and  $\mu^2 = 2.82 \pm 0.290 \text{ GeV}^2$ .

parameters	value
$a_{00}$	$2.550 \times 10^{-1} \pm 1.60 \times 10^{-2}$
$a_{01}$	$1.475 \times 10^{-1} \pm 3.025 \times 10^{-2}$
$a_{10}$	$8.205 \times 10^{-4} \pm 4.62 \times 10^{-4}$
$a_{11}$	$-5.148 \times 10^{-2} \pm 8.19 \times 10^{-3}$
$a_{12}$	$-4.725 \times 10^{-3} \pm 1.01 \times 10^{-3}$
$a_{20}$	$2.217 \times 10^{-3} \pm 1.42 \times 10^{-4}$
$a_{21}$	$1.244 \times 10^{-2} \pm 8.56 \times 10^{-4}$
$a_{22}$	$5.958 \times 10^{-4} \pm 2.32 \times 10^{-4}$
$n$	$11.49 \pm 0.99$
$\lambda$	$2.430 \pm 0.153$
$\chi^2(\text{goodness of fit})$	0.95

TABLE III: The QCD coupling and corresponding  $\Lambda$  parameter for  $n_f = 4$  at LO, NLO [12, 25] and NNLO analysis [26].

	$\alpha_s(M_Z^2)$	$\Lambda_{QCD}(MeV)$
LO	0.1166	136.8
NLO	0.1166	284
NNLO	0.1155	235

## REFERENCES

1. M.Kuroda and D.Schildknecht, Phys.Lett. **B618**, 84(2005); M.Kuroda and D.Schildknecht, Acta Phys.Polon. **B37**, 835(2006).
2. M.Kuroda and D.Schildknecht, Phys.Lett. **B670**, 129(2008); M.Kuroda and D.Schildknecht, Phys.Rev. **D96**, 094013(2017).
3. D.Schildknecht and M.Tentyukov, arXiv[hep-ph]:0203028; M.Kuroda and D.Schildknecht, Phys.Rev. **D85**, 094001 (2012).
4. D.Schildknecht, Mod.Phys.Lett.A**29**, 1430028(2014).
5. M.Kuroda and D.Schildknecht, Int. J. Mod. Phys. **A31**, 1650157 (2016).
6. Amir H.Rezaeian and I.Schmidt, Phys.Rev. **D88**, 074016 (2013).
7. H.Abramowicz et al.,[H1 and ZEUS Collaborations], Eur.Phys.J.C**75**, 580(2015).
8. M.Klein, arXiv [hep-ph]:1802.04317.
9. N.Armesto et al., arXiv [hep-ph]:1901.09076.
10. A. Abada et al., [FCC Collaborations], Eur.Phys.J.C**79**, 474(2019).
11. J.R.Forshaw et al., JHEP **0611**, 025(2006).



12. M. M. Block, L. Durand and P. Ha, Phys. Rev.D **89**, no. 9, 094027 (2014).
13. Yu.L.Dokshitzer, Sov.Phys.JETP **46**, 641(1977); G.Altarelli and G.Parisi, Nucl.Phys.B **126**, 298(1977); V.N.Gribov and L.N.Lipatov, Sov.J.Nucl.Phys. **15**, 438(1972).
14. V.S.Fadin, E.A.Kuraev and L.N.Lipatov, Phys.Lett.B **60**, 50(1975); L.N.Lipatov, Sov.J.Nucl.Phys. **23**, 338(1976); I.I.Balitsky and L.N.Lipatov, Sov.J.Nucl.Phys. **28**, 822(1978).
15. G.R.Boroun and B.Rezaei, Nucl.Phys.A**990**, 244(2019).
16. B.Rezaei and G.R.Boroun, Eur.Phys.J.A**55**, 66(2019).
17. S.Moch, J.A.M.Vermaseren, A.Vogt, Phys.Lett.B **606**, 123(2005).
18. V.Andreev et al. [H1 Collaboration], Eur.Phys.J.C**74**, 2814 (2014).
19. S.Moch, J.A.M.Vermaseren, A.Vogt, Phys.Lett.B **606**, 123(2005).
20. W.L. van Neerven, A.Vogt, Phys.Lett.B **490**, 111(2000).
21. A.Vogt, S.Moch, J.A.M.Vermaseren, Nucl.Phys.B **691**, 129(2004).
22. G.R.Boroun, Phys.Rev. **C97**, 015206 (2018); G.R.Boroun and B.Rezaei, Eur.Phys.J. **C72**, 2221 (2012).
23. L.P.Kaptari et al., Phys.Rev.D**99**, 096019(2019).
24. F. D. Aaron et al. [H1 and ZEUS Collaborations], JHEP**1001**, 109 (2010).
25. S. Chekanov et al. [ZEUS Collaboration], Eur. Phys. J. **C21**, 443 (2001).
26. A.D.Martin et al., Phys.Letts.**B604**, 61(2004).
27. K Golec-Biernat and A.M.Stasto, Phys.Rev.D **80**, 014006(2009).
28. G.R.Boroun, arXiv[hep-ph]:1903.04316; G.R.Boroun and B.Rezaei, Eur.Phys.J. **C73**, 2412 (2013); Phys.Atom.Nucl.**71**, 1077 (2008); EPL**100**, 41001 (2012).
29. A. Y. Illarionov, A. V. Kotikov and G. Parente Bermudez, Phys. Part. Nucl. **39**, 307 (2008).
30. C.Ewerz et al., Phys.lett.B**720**, 181(2013).
31. C.Ewerz and O.Nachtmann, Phys.Lett.B**648**, 279(2007).
32. M.Niedziela and M.Praszalowicz, Acta Phys.Polon. B**46**, 2019(2015).
33. V.Tvaskis et al., Phys.Rev.**C97**, 045204(2018); Phys.Rev.Lett. **98** (2007) 142301.
34. F.D. Aaron et al. [H1 Collaboration], phys.Lett.B**665**, 139(2008); Eur.Phys.J.C**71**,1579(2011).
35. C.Ewerz et al., Phys.Rev. D**77**, 074022 (2008).
36. H.Abromowicz et al. [ZEUS Collaboration], Phys.Rev.D**9**, 072002(2014).
37. A. Donnachie, P.V. Landshoff, Phys. Lett. B **550**, 160 (2002); B.Rezaei and G.R.Boroun , Int.J.Theor.Phys. **57**, 2309 (2018).
38. Martin M. Block et al., Phys. Rev. D **84** , 094010 (2011).
39. M. Praszalowicz, Phys. ReV. Lett. **106**, 142002 (2011).
40. M. Praszalowicz, T. Stebel, JHEP**03**, 090 (2013).
41. H1 and ZEUS Collaboration (F.D. Aaron et al.), JHEP **01**, 109 (2010); H1 and ZEUS Collaboration (F.D. Aaron et al.), Eur. Phys. J. C **63**, 625 (2009); H1 and ZEUS Collaboration (F.D. Aaron et al.), Eur. Phys. J. C **64**, 561 (2009).
42. A. H. Mueller and J. Qiu, Nucl. Phys. B**268**(1986)427; L. V. Gribov, E. M. Levin and M. G. Ryskin, Phys. Rep.**100**, (1983)1.
43. G.R.Boroun and S.Zarrin, Eur.Phys.J.Plus **128**, 119(2013); G. R. Boroun and B. Rezaei, Chin. Phys. Lett.**32**, (2015) no.11, 111101; B. Rezaei and G. R. Boroun, Phys. Lett. **B692** (2010) 247; G. R. Boroun, Eur. Phys. J. A**43** (2010) 335; G.R.Boroun, Eur.Phys.J. A**42**, 251 (2009).
44. M.Devée, arXiv[hep-ph]:1808.00899; M.Devée and J.K.sarma, Nucl.Phys. **B885**, 571(2014); M.Lalung et al., Nucl.Phys. **A984**, 29 (2019); P.Phukan et al., Nucl.Phys. **A968**, 275 (2017).
45. R.Wang and X.Chen, Chin.Phys. **C41**, 053103 (2017); J.Lan et al., arXiv[nucl-th]:1907.01509.
45. N. N. Nikolaev and W. Schäfer, Phys. Rev. D**74**(2006)014023.
46. K. J. Eskola et al., Nucl. Phys. B**660**(2003)211.
47. R. Fiore, P. V. Sasorov and V. R. Zoller, JETP Letters **96**(2013)687; R. Fiore, N. N. Nikolaev and V. R. Zoller, JETP Letters **99**(2014)363.

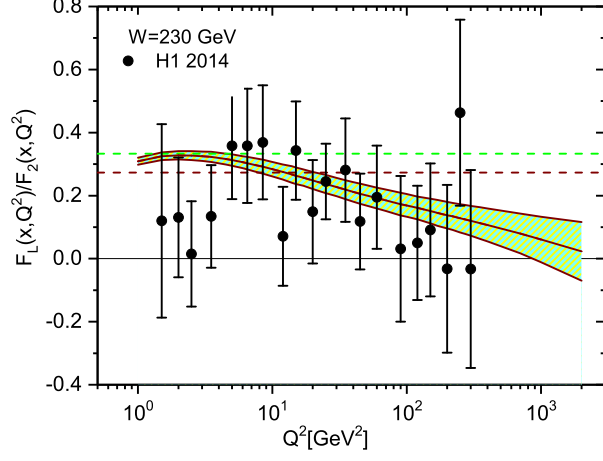


FIG. 1: The ratio  $F_L/F_2$  extracted at NNLO approximation in comparison with the H1 data [16] as accompanied with total errors. The results are presented at fixed value of the invariant mass  $W$  in the interval  $1 \text{ GeV}^2 \leq Q^2 < 3000 \text{ GeV}^2$  at low values of  $x$ . The shaded are corresponds to uncertainties of the  $F_2$  parameterization (i.e., Table II). The dipole upper bounds (i.e., Eqs.(13) and (20)) represented by the dashed lines respectively.

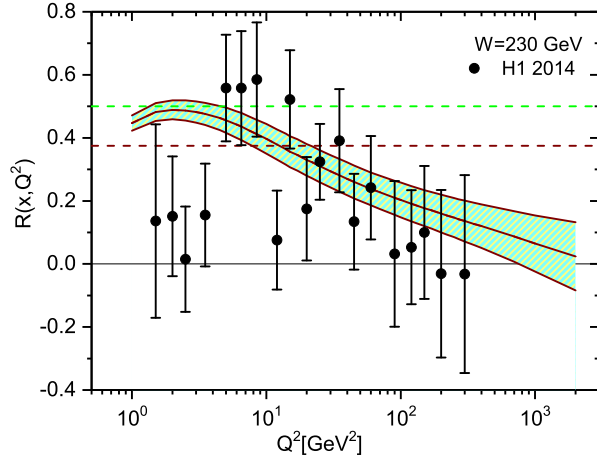


FIG. 2: The same as Fig.1 for the ratio  $R$ .

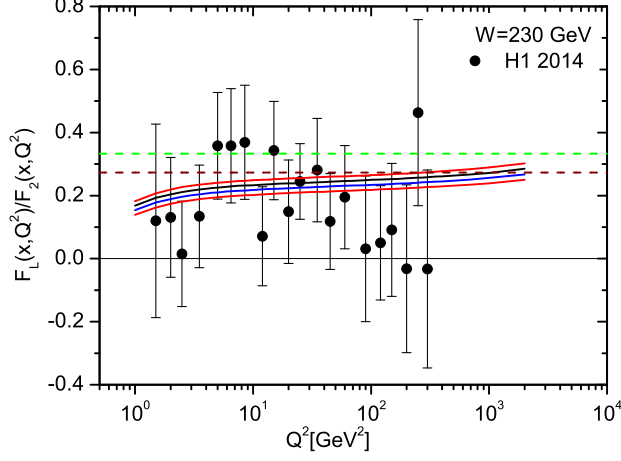


FIG. 3: The ratio  $F_L/F_2$  extracted at NNLO approximation in comparison with the H1 data [16] as accompanied with total errors. The results are presented at fixed value of the invariant mass  $W$  in the interval  $1 \text{ GeV}^2 \leq Q^2 < 3000 \text{ GeV}^2$  at low values of  $x$ . The solid lines are defined with the fixed exponents. The exponents  $\lambda$ 's are a dynamical quantity of the order of  $\lambda = 0.27, 29, 31$  and  $0.33$  from lower to upper curves respectively. The dipole upper bounds (i.e., Eqs.(13) and (20)) represented by the dashed lines respectively.

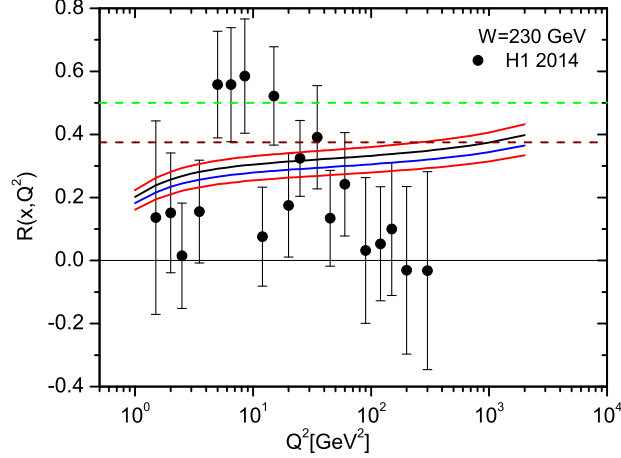


FIG. 4: The same as Fig.3 for the ratio  $R$ .

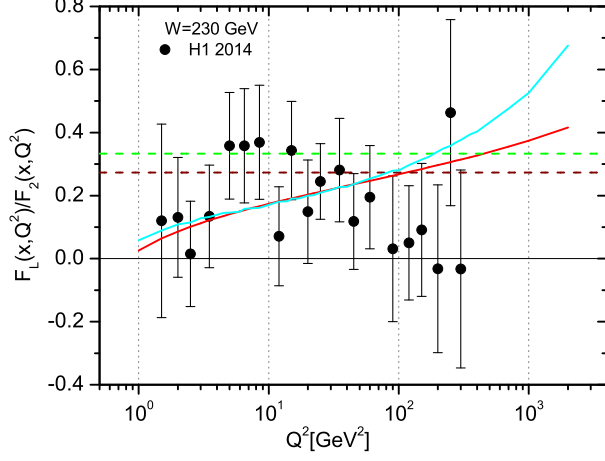


FIG. 5: The ratio  $F_L/F_2$  extracted at NNLO approximation in comparison with the H1 data [16] as accompanied with total errors. The results are presented at fixed value of the invariant mass  $W$  in the interval  $1 \text{ GeV}^2 \leq Q^2 < 3000 \text{ GeV}^2$  at low values of  $x$ . The solid lines are defined with the effective exponents. The exponents  $\lambda(Q^2)$  are parameterized with respect to Eqs.(41) and (42) from lower to upper curves respectively. The dipole upper bounds (i.e., Eqs.(13) and (20)) represented by the dashed lines.

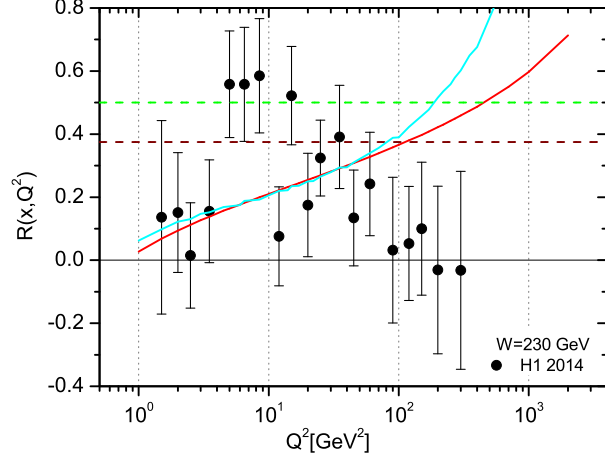


FIG. 6: The same as Fig.5 for the ratio  $R$ .

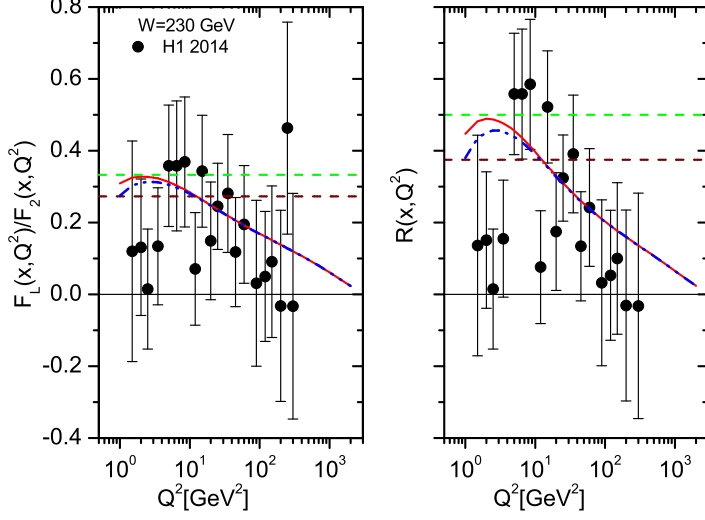


FIG. 7: The nonlinear corrections to the ratio  $F_L/F_2$  and  $R$  extracted at NNLO approximation in comparison with the H1 data [16] as accompanied with total errors. The results are presented at fixed value of the invariant mass  $W$  in the interval  $1 \text{ GeV}^2 \leq Q^2 < 3000 \text{ GeV}^2$  at low values of  $x$ . The dash-dot line is defined with the nonlinear corrections in comparison with the linear (i.e., solid line). The dipole upper bounds (i.e., Eqs.(13) and (20)) represented by the dashed lines respectively.

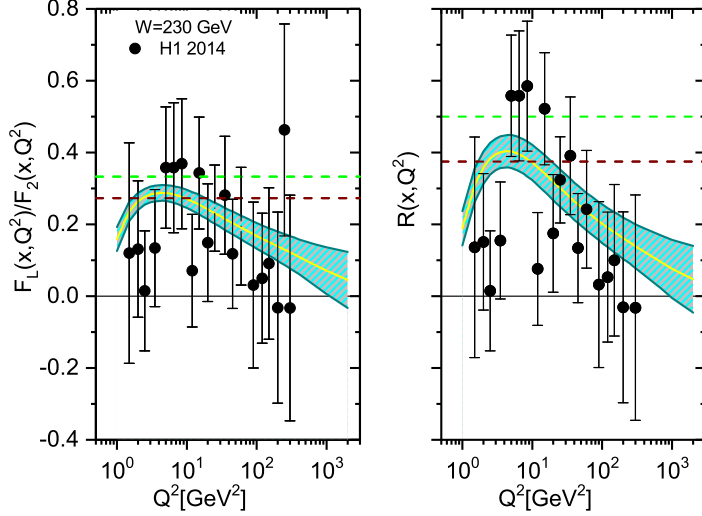


FIG. 8: The nonlinear corrections to the ratio  $F_L/F_2$  and  $R$  with the effective exponent  $\lambda(Q^2)$  [40] extracted at NNLO approximation in comparison with the H1 data [16] as accompanied with total errors. The results are presented at fixed value of the invariant mass  $W$  in the interval  $1 \text{ GeV}^2 \leq Q^2 < 3000 \text{ GeV}^2$  at low values of  $x$ . The error bands represent the uncertainty estimation coming from the  $F_2$  parameterization. The dipole upper bounds (i.e., Eqs.(13) and (20)) represented by the dashed lines respectively.